Catalysis Today 301 (2018) 25–31

Contents lists available at ScienceDirect

Catalysis Today

journal homepage: www.elsevier.com/locate/cattod

# Template growth of nitrogen-doped mesoporous graphene on metal oxides and its use as a metal-free bifunctional electrocatalyst for oxygen reduction and evolution reactions

Hao-Fan Wang, Cheng Tang, Qiang Zhang*

*Beijing Key Laboratory of Green Chemical Reaction Engineering and Technology, Department of Chemical Engineering, Tsinghua University, Beijing 100084, China*

ARTICLE INFO

*Article history:*
Received 15 November 2016
Received in revised form 12 January 2017
Accepted 9 February 2017
Available online 21 February 2017

*Keywords:*
Graphene
Oxygen reduction reaction
Oxygen evolution reaction
Metal-free electrocatalyst
Doped carbon
Carbocatalysis

ABSTRACT

Metal-free electrocatalyst is an emerging energy material to replace precious metal for effective oxygen reduction reaction (ORR) and oxygen evolution reaction (OER) in a working electrochemical energy conversion device. Developing an effective bifunctional catalyst with abundant highly active sites and full exposure to reactants is strongly considered. Herein a nitrogen-doped mesoporous graphene framework (NMGF) was proposed with intrinsic N/O heteroatoms and abundant topological defects for metal-free ORR/OER. The NMGF was fabricated by direct chemical vapor deposition on MgO template. The as-obtained NMGF exhibited high porosity with a large specific surface area of 1440 $m^2 g^{-1}$ as well as a high electrical conductivity of 57.0 S $cm^{-1}$. This unique structure is demonstrated to possess several advantages, including plentiful active centers due to defects and heteroatoms, improved utilization efficiency by very high electrochemically active surface area and hydrophilic surface, facilitated ion diffusion through interconnected pores and smooth electron transportation in the highly conductive 3D framework, thereby leading to superior ORR and OER bifunctional activity. The ORR half-wave potential was 0.714 V, and the potential to reach 10.0 mA $cm^{-2}$ OER current density was 1.664 V with the potential gap of 0.95 V. This bifunctional performance was better than routine precious metal-based catalysts (*e.g.* Pt/C and $IrO_2$) for oxygen redox reaction.



## 1. Introduction

The urgent request to solve the energy crisis and environmental problems brings great interests in clean, renewable energy sources, and emerging energy storage devices, like solar cells, hydrogen fuel cells, and metal-air batteries. One critical issue in the related sustainable chemistry is the transformation between water and oxygen, including oxygen reduction reaction (ORR) and oxygen evolution reaction (OER) [1–4]. Both ORR and OER are 4-electron processes, suffering from their sluggish kinetics and high overpotential, which strongly limit the efficiency of relative energy devices. This calls for efficient electrocatalysts for ORR and OER [5–7]. In some particular cases like rechargeable metal-air batteries, ORR and OER are required to occur on the same electrode during the charge and discharge process, respectively [8–10]. Therefore, the bifunctional electrocatalysis of ORR and OER is of great significance [8,11].

Precious metals and their oxides are effective electrocatalysts in these reactions, including Pt and PtRu for ORR [12,13] and Ir and $IrO_2$ for OER [14–16]. However, the high cost and limited natural abundance of the precious metals obstruct their large-scale applications, and the precious metal catalysts usually afford poor activity in bifunctional catalysis [17,18]. In recent years, the research and development of non-precious metal bifunctional catalysts for ORR and OER has been strongly considered. Catalysts based on transition metal compounds were firstly investigated, and Co- and Mn-based high-performance bifunctional catalysts were reported [19–22]. In 2014, Tian et al. [23] proposed a metal-free nanocarbon catalyst with remarkable activity on both ORR and OER. Since then, increasingly more carbon nanomaterials were reported as ORR/OER bifunctional catalysts attributed to their various, controllable structure and high electrical conductivity [11,24–28]. During the researches on carbon nanomaterials for ORR/OER electrocatalysis, two kinds of structural configurations, heteroatom and defect, have attracted much attention and been demonstrated as active sites [26,27,29–32].

To take full advantage of the active sites and facilitate the oxygen transport, the metal-free carbon based electrocatalyst is

* Corresponding author.
*E-mail address:* zhang-qiang@mails.tsinghua.edu.cn (Q. Zhang).

http://dx.doi.org/10.1016/j.cattod.2017.02.012
0920-5861/

preferred to be highly porous, which always results in a defective structure with high electrical resistance [33–35]. In the electrocatalysis of ORR and OER, however, the gas transport in the pore and electron transport in the electrode are both important issues. More understandings are required to rationally design an effective electrocatalyst with intrinsic ORR/OER reactivity as well as full exposure of active centers to electrolyte.

In order to balance the porosity and electrical conductivity in nanocarbon electrocatalysts with intrinsic reactivity for ORR/OER, a 3D metal-free nanocarbon with interconnected pores constructed by continuous graphene layers was proposed herein. This energy material, named as N-doped mesoporous graphene framework (NMGF), presents a highly porous morphology with high conductivity, and possesses both kinds of active sites: the heteroatom (nitrogen) and the defect (five- and seven-carbon rings, C5 and C7) derived from the curves of the graphene. Besides, the unique structure of NMGF significantly contributes to the full accessibility of active sites for ORR/OER. Consequently, the as-fabricated NMGF material is demonstrated to be a superior metal-free bifunctional electrocatalyst for both ORR and OER.

## 2. Experimental

### 2.1. Material synthesis

The NMGF was synthesized using chemical vapor deposition (CVD) method with mesoporous MgO as template [36,37] and methane/ammonia as carbon/nitrogen source. 0.50 g MgO template was dispersed uniformly into a quartz boat and then placed in the center of a horizontal quartz tube reactor. The tube was then inserted into a furnace at atmospheric pressure. Under the protection of Ar at a flow rate of 200 mL $min^{-1}$, the quartz reactor was heated to 950 °C, and then both $CH_4$ (50 mL $min^{-1}$) and $NH_3$ (40 mL $min^{-1}$) were introduced into the reactor for 10 min. After the CVD growth of NMGF, the furnace was cooled to room temperature in the atmosphere of $H_2$ (10 mL $min^{-1}$) and Ar. The product was then mixed with 500 mL of 6 mol $L^{-1}$ HCl and heated in oil bath at 80 °C for 24 h to remove the MgO template. The acid was washed off by deionized water during a vacuum filtering process. Finally, the filter cake was dried by a freeze-drying method to obtain the NMGF sample. MGF was prepared in a similar way in which ammonia was not introduced in the CVD growth.

To verify the role of pore structure and defects in the NMGF, a control sample N-doped graphene (NG) was synthesized from chemical reduction of graphene oxide (GO). 30 mL of 2.0 mg $mL^{-1}$ GO aqueous solution was mixed with 1.80 g urea by 30 min ultrasonic dispersion. Then the suspension was treated by hydrothermal method at 180 °C for 18 h. After the vacuum filtering, washing, and freeze-drying, the NG sample was achieved.

### 2.2. Structural characterization

The morphology of the graphene-based electrocatalsyts was characterized using a JSM 7401F scanning electron microscope (SEM) operated at 3.0 kV and a JEM 2010 high-resolution transmission electron microscope (TEM) operated at 120.0 kV. The Brunauer–Emmett–Teller (BET) specific surface area (SSA) of the samples was probed by $N_2$ adsorption/desorption at liquid-$N_2$ temperature using Autosorb-IQ2-MP-C system. The specific surface area was calculated by the multipoint Brunauer–Emmett–Teller (BET) method with the relative pressure of 0.05–0.30, and the pore-size distribution was calculated based on quenched solid density function theory model using the adsorption branch. The electrical conductivity of plate-samples with a diameter of 13.0 mm and a thickness of *ca.* 10 μm, which were prepared by compression at 10.0 MPa, was measured using ST-102A four-probe technique (4Probes Tech., China) with Keithley 2636A Source Meter. The amounts of N-containing functional groups on NMGF were identified using X-ray photoelectron spectroscopy (XPS) by Escalab 250xi. Raman spectra were obtained using a Horiba Jobin Yvon LabRAM HR800 Raman spectrophotometer with He–Ne laser excitation at 633 nm. The contact angle was collected on Dataphysics OCA20. A volume of the pure water droplet employed in the measurement was 2 μL.

### 2.3. Electrochemical characterization

All electrochemical measurements were performed in a three-electrode system, using Pt sheet as a counter electrode and saturated calomel electrode (SCE) as a reference electrode. Rotating ring-disk electrode (RRDE) coated with electrocatalyst was used as the working electrode. This three-electrode system was controlled by a CHI 760D electrochemistry workstation and the measurements were carried out in $O_2$-saturated 0.10 M KOH solution. Before other measurements were applied, the catalyst was cycled several times by cyclic voltammetry (CV) to obtain a stable CV curve. The OER and ORR activities were tested by linear sweep voltammetry (LSV) at the scan rate of 10.0 mV $s^{-1}$.

The working electrode was fabricated by a drop casting method. 5.0 mg catalyst was dispersed in 0.95 mL ethanol and 0.05 mL 5.0 wt.% Nafion solution by 1.0 h sonication to form a relatively uniform suspension. Then 10.0 μL of the catalyst suspension was transferred onto the glass carbon electrode (GC, 0.196 $cm^2$) *via* a controlled drop casting approach. The electrode was finally dried by natural evaporation. In addition to the three carbon materials, two commercial precious metal catalysts were also used as contrast samples: Pt/C catalyst with 20 wt.% Pt (Sigma–Aldrich), and 99.99% $IrO_2$ catalyst (Alfa Aesar).

The ORR electron transfer number $n$ was determined as followed:

$$n = \frac{4I_d}{I_d + I_r/N}$$

where $I_d$ is disk current, $I_r$ is ring current and $N$ is current collection efficiency of the Pt ring which was determined to be 0.26.

Electrochemical active surface area (ECSA) was determined by measuring the capacitive current associated with double-layer charging from the scan-rate dependence of cyclic voltammetry (CV). This measurement was performed on the same working electrodes among a potential window of 0.95–1.05 V *vs.* reversible hydrogen electrode (RHE) and scan rates ranging from 20 to 100 mV $s^{-1}$. Then linear fitting of the charging current density differences ($\Delta j = j_a - j_c$ at the potential of 1.00 V *vs.* RHE) against the scan rate was done. The slope is twice of the double-layer capacitance $C_{dl}$, which is used to represent ECSA.

The potential *vs.* RHE ($E_{vs.\ RHE}$) was calculated by the following equation: $E_{vs.\ RHE} = E_{vs.\ SCE} + 0.059\ pH + 0.241$ ($E_{vs.\ SCE}$ stands for the potential *vs.* SCE) and the overpotential $\eta = E_{vs.\ RHE} - 1.23$.

## 3. Results and discussion

### 3.1. The NMGF grown on MgO templates

The morphology and synthesis method of NMGF are illustrated in Fig. 1. The MgO template is composed by closely packed nanocrystals with a size of 4–8 nm (Fig. 1a). The 3D graphene was deposited on the surface of the MgO template (Fig. 1b) during CVD growth. After the template was etched by HCl, the graphene framework with abundant mesopores and continuous graphene layers was achieved (Fig. 1c).

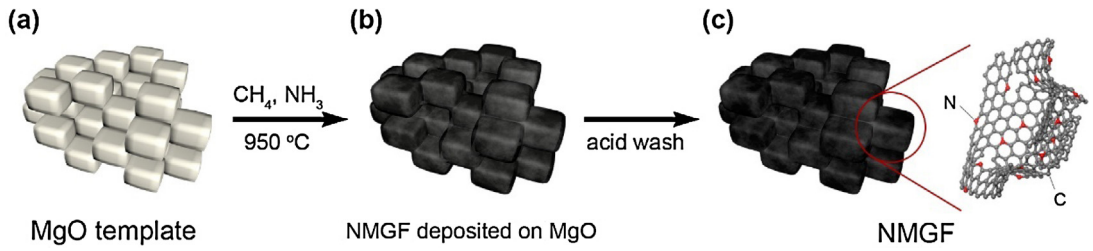


**Fig. 1.** The scheme of NMGF formation on porous MgO template.

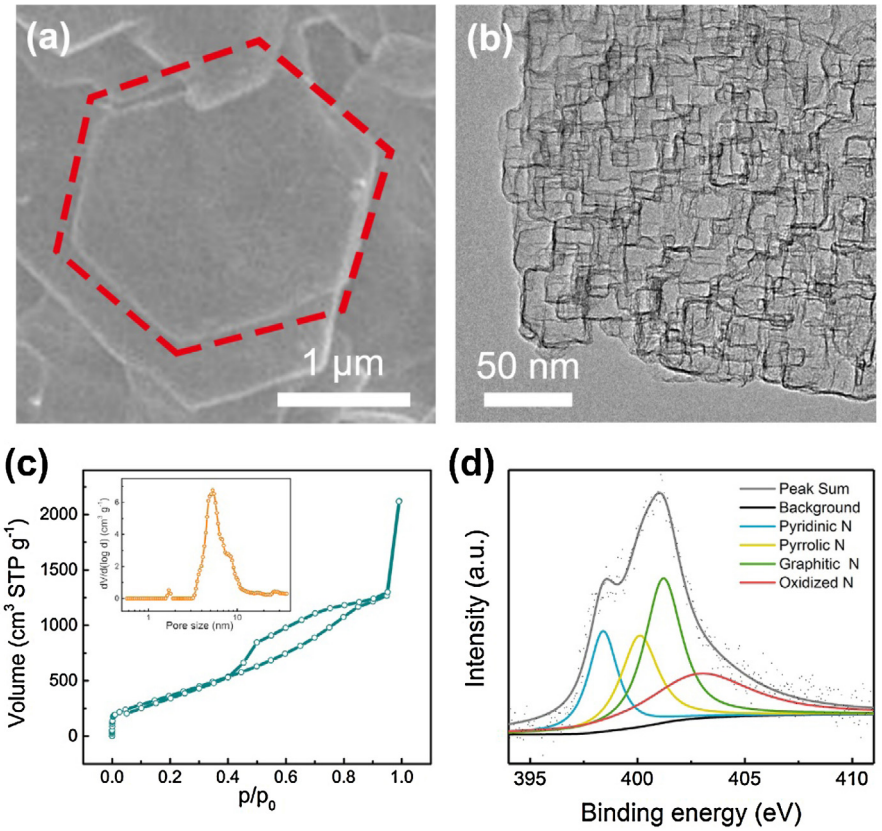


**Fig. 2.** Characterization of metal-free NMGF electrocatalyst. (a) SEM and (b) TEM images of NMGF. (c) Nitrogen adsorption–desorption isotherm of NMGF. STP is short for standard temperature and pressure. Inset: Pore distribution of NMGF. (d) High-resolution XPS spectrum of N 1s core levels in NMGF.

NMGF sheets are hexagon with a diameter of about 2 μm and a thickness of around 50 nm (Fig. 2a). Interconnected mesopores are observed on a NMGF sheets by TEM (Fig. 2b). Besides, NGMF is mainly constructed by single/few-layer curve graphene nanosheets. The scene of overlapped pores with regular shape is just like a Mondrian painting. In addition, there are abundant edges and curves in the NMGF, which can be widely observed in TEM images and are supposed to generate C5 and C7 defects [38].

The nitrogen adsorption–desorption isotherm curve (Fig. 2c) verifies the porosity of NMGF. There are abundant mesopores between 2 and 10 nm in the pore size distribution profile. The SSA calculated by multipoint BET method was 1440 $m^2 g^{-1}$. The four-point probe method reveals that the electrical conductivity of NMGF is *ca.* 57.0 S $cm^{-1}$.

The total content of nitrogen heteroatoms in the NMGF is calculated to be 3.41 at.% based on the XPS method. The N1s spectrum of NMGF is resolved into four peaks (Fig. 2d). The pyridinic N (18.0 at.%), pyrrolic N (20.8 at.%), quaternary N (32.9 at.%), and oxidized N (28.3 at.%), with the bonding energy at 398.4, 400.1, 401.2, and 402.9 eV, respectively, are confirmed.

Based on the above characterizations, the NMGF exhibits unique features of N-doping and defect-rich, resulting in the intrinsic activity of NMGF for OER and ORR. Accompanied by the pore structure and high electrical conductivity that enhance the gas transport and electron transport, respectively, the NMGF is expected to be a promising catalyst in the ORR/OER bifunctional electrocatalysis.

### 3.2. ORR/OER performances on NMGF

The electrochemical tests were performed in $O_2$-saturated 0.10 M KOH electrolyte with a three-electrode system. Besides commercial $IrO_2$ and Pt/C catalysts, non-doped MGF and N-doped graphene (NG, synthesized from reduction of graphene oxide, see details in Section 2) are chosen as the control electrocatalysts. The MGF and NG were also characterized by SEM and TEM (Fig. S1), physical absorption (Fig. S2) and XPS (Fig. S3). For the three carbon nanomaterials, the pore structure information (specific surface area and pore volume), and the elemental composition measured by XPS are listed in Tables S1 and S2, respectively. The MGF has the same microstructure as NMGF, but lacks the nitrogen heteroatoms.

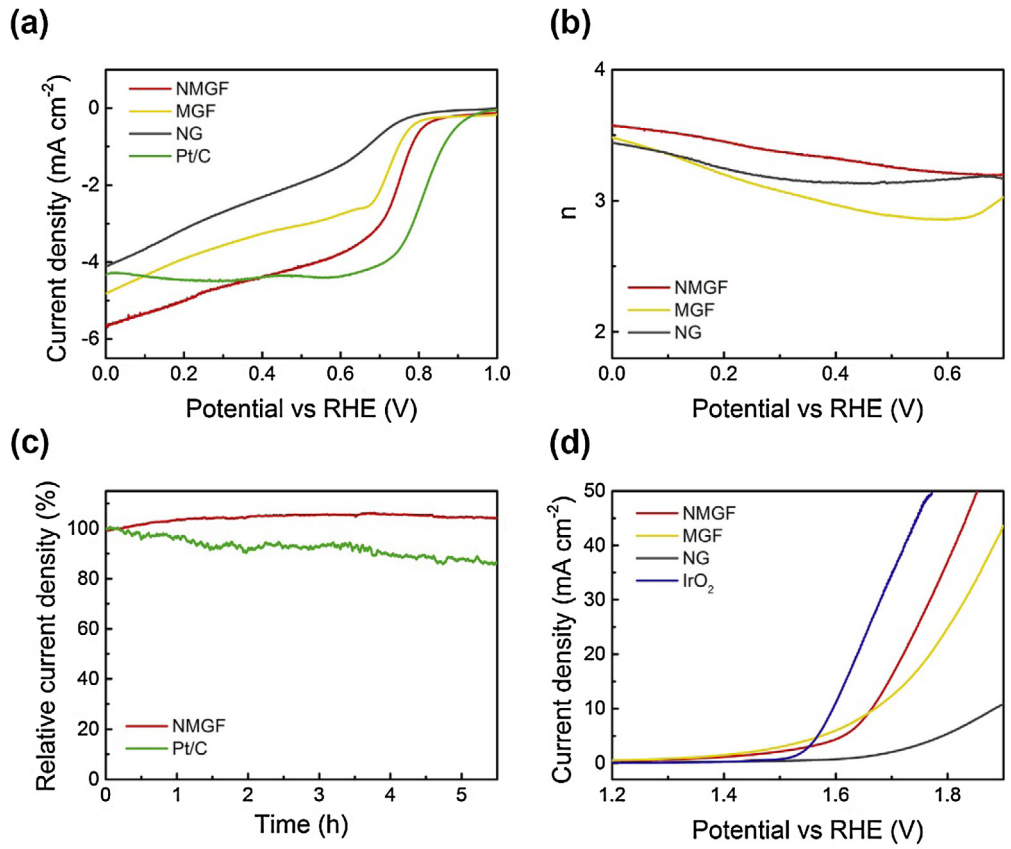


**Fig. 3.** The electrochemical performances of metal-free electrocatalysts. (a) The ORR LSV plots of NMGF, MGF, NG, and Pt/C at a scan rate of 10.0 mV $s^{-1}$. (b) The ORR electron transfer number of NMGF, MGF, and NG. (c) The ORR stability of NMGF and Pt/C. The stability was measured using a potentiostatic method with the initial current density of 1.0 mA $cm^{-2}$. (d) The OER LSV plots of NMGF, MGF, NG, and $IrO_2$ with the scan rate of 10.0 mV $s^{-1}$. All the tests were operated in $O_2$-saturated 0.10 M KOH electrolyte.

In contrast, NG consists of abundant nitrogen heteroatoms, but is less porous than NMGF. In other words, in MGF, the active sites are mainly topological defects (*e.g.* C5 and C7) attributed to the curving graphene structure; while in NG, the active sites are mainly contributed from the heteroatoms. Contrastively, NMGF possesses both kinds of potential active sites.

The electrocatalytic reactivity of ORR/OER on NMGF, MGF, and NG is shown in Fig. 3. As shown in the ORR linear sweep voltammetry (LSV) plots (Fig. 3a), NMGF exhibits superior ORR activity compared with MGF and NG. The ORR half-wave potential ($E_{1/2}$) of NMGF is 0.714 V *vs.* RHE, much better than 0.685 V for MGF and 0.521 V for NG. In our recent study [27], the activity of graphene defects and nitrogen heteroatoms was investigated by density functional theory (DFT) approach. Both C5 and C7 defects and the doped N atoms were demonstrated to contribute to the ORR activity. Therefore, NMGF with both kinds of active sites affords better ORR performance than MGF. The superiority of MGF to NG is attributed to the unique porous and conductive structure of the graphene framework. The ORR electron transfer number ($n$) plotted in Fig. 3b is also in line with the order of NMGF > MGF > NG. Moreover, the ORR Tafel plots (Fig. S4) indicate more favorable kinetics of NMGF than MGF and NG, even slightly better than Pt/C.

In order to determine the stability of NMGF, a long-time potentiostatic test of NMGF and the commercial Pt/C was performed at the initial current density of 1.0 mA $cm^{-2}$ (Fig. 3c). Pt/C catalyst only maintained 85% of the initial current density after 5 h test. On the contrary, the current density of NMGF was even slightly increased, probably due to the infiltration of the electrolyte to more pores in the NMGF.

The OER LSV plots are exhibited in Fig. 3d. The potential to obtain 10.0 mA $cm^{-2}$ OER current density ($E_{10}$) for NMGF, MGF, and NG is 1.664, 1.671, and 1.885 V, respectively. It was claimed that the C5 and C7 defects outperformed N heteroatoms significantly in the OER region [27]. As expected, MGF exhibited similar OER activity to NMGF in spite of the absence of N-doping; while NG was almost inactive for OER due to the lack of topological defects.

The bifunctional activity of the catalysts can be evaluated by the potential gap ($\Delta E$) between $E_{1/2}$ and $E_{10}$ [39–41]. The $\Delta E$ of NMGF is determined to be 0.95 V, surpassing MGF (0.99 V) and NG (1.36 V), and furthermore, better than commercial $IrO_2$ (1.53 V) and Pt/C (1.28 V). Based on the experimental results, we can identify NMGF as a remarkable metal-free bifunctional electrocatalyst for ORR and OER, with promising applications for metal-air batteries and fuel cells.

### 3.3. Discussion on the superb ORR/OER activity on NMGF

Both ORR and OER catalysis on the electrode are complicated processes involving gas transport, surface reaction, electron conduction, and ion diffusions. An effective electrocatalyst of the oxygen electrode is supposed to render active centers with high intrinsic activity, and those active sites are expected to be fully exposed during the oxygen redox reaction.

In this contribution, the NMGF electrocatalyst possesses two kinds of active sites. The first one is the N/O heteroatom. From the elemental analysis data of NMGF, MGF, and NG measured by XPS (Fig. S3 and Table S2), the nitrogen atomic contents of NMGF MGF, and NG are 3.41, 0.34, and 5.31 at.%, respectively, and the oxygen content in NMGF, MGF, and NG are 3.34, 1.53, and 5.19 at.%,

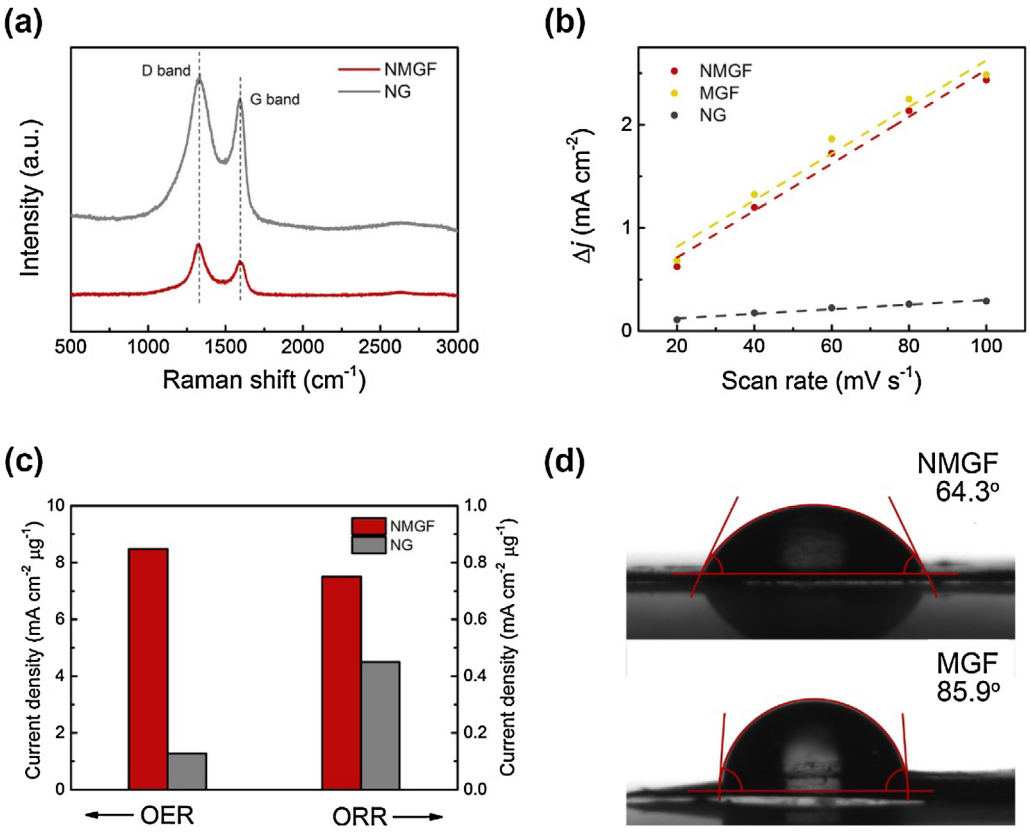


**Fig. 4.** The analysis of OER/ORR reactivity on NMGF electrocatalyst. (a) Raman spectra of NMGF and NG. (b) Charging current density differences plotted against scan rates. The linear slope, equivalent to twice the double-layer capacitance $C_{dl}$, was employed to represent the ECSA. (c) The specific current density of NMGF and NG based on nitrogen mass, tested at the potential of 1.80 V *vs.* RHE (OER) and 0.50 V *vs.* RHE (ORR). (d) The contact angles of NMGF and MGF.

respectively. The doping of nitrogen heteroatoms with a larger electronegativity induces a substantially positive charge density on the adjacent carbon atoms [42], which is widely accepted as the active centers of nitrogen doped carbon electrocatalysts for ORR in alkali solution [43]. As shown in Fig. 2d, NMGF mainly consists of graphitic N, while the majority of N dopants in NG is pyridinic N (Fig. S5), probably due to the different synthesis methods of the two materials. Based on our former work [27], graphitic N is more active for OER, while pyridinic N is a better active site for ORR. This corresponds well with the poor OER activity and relatively better ORR activity of NG. Furthermore, the addition of oxygen dopants break the electroneutrality of $sp^2$ carbon lattice and therefore afford an enhanced ORR activity [44]. However, the ORR and OER activity contributed by single oxygen-doping is quite limited [45,46], and oxygen dopants would not have much effect on the catalytic activity if there are no other heteroatoms in the metal-free carbon electrocatalyst [5].

The second kind of active sites in NMGF is the topological C5 and C7 defects induced by the graphene curves. To confirm the defect-rich feature of the NMGF structure, the Raman spectra of NMGF and NG was tested and plotted in Fig. 4a. The higher $I_D/I_G$ ratio of NMGF compared with NG (1.39 *vs.* 1.16) indicates more defects in NMGF. It is accepted that the pentagon and zigzag edges decrease the ORR reaction free energy and facilitate the electron transfer for OOH* [29]. A nitrogen-free intrinsic defect of adjacent pentagon and heptagon was identified as the best configuration for both ORR and OER. The adjacent carbon rings with different electron densities induce spatial curvatures and form a permanent dipole moment. The dipole moment is weaker than the one between nitrogen and carbon atoms, which facilitates the facile ORR/OER on defect-rich carbon electrocatalysts [27,47]. In the Raman spectrum of MGF (Fig. S6), the $I_D/I_G$ ratio (2.17) is even higher than NMGF, which may due to the higher surface area and more exposed defects of MGF. However, a large quantity of defects in MGF may not be available in the electrocatalysis process, because MGF has poor hydrophilicity thus the surface can hardly expose to the electrolyte. This will be discussed in detail in the following part.

Besides the intrinsic activity of the active sites, the structural features of NMGF can further facilitate the exposure of active sites, thus enhancing the activity of a working electrode. On one hand, the continuous pore structure enlarges the surface area and benefits the gas transport. The ECSA correlated to the double layer capacity ($C_{dl}$) represents the contact area of the electrocatalyst and electrolyte under working condition. The $C_{dl}$ was obtained by CV method in a potential range without pseudo-reactions. The difference of the charging current density and the discharging current density, $\Delta j$, is a linear function of the CV scan rate (Fig. 4b). The slope is twice $C_{dl}$, which is proportional to the ECSA. The ECSA of NMGF is about ten times of that of NG at the same areal loading. This result indicates more contact between the electrolyte and the catalyst for NMGF, suggesting a higher utilization efficiency of the active sites.

The sufficient use of active sites in NMGF can also be identified by calculating the specific current density based on the mass of nitrogen in the catalyst as the benchmark. The activity of NG is provided mainly by the nitrogen doping, but the defects also contribute a lot in NMGF. Herein, the N-contributed activity of NMGF is approximated by subtracting the MGF current density from the NMGF current density. According to the results in Fig. 4c, the ORR and OER mass specific current densities both verify the superior utilization efficiency of active sites on NMGF electrocatalyst compared with NG. This advantage is largely attribute to its novel structure, as characterized above.

On the other hand, the N-doping in NMGF improves the hydrophilicity, therefore exposes more active centers to the electrolyte. In BET surface area values of NMGF, MGF and NG measured by $N_2$ adsorption–desorption isothermal method listed in Table S1, the SSA of NMGF ($1440\ m^2\ g^{-1}$) is smaller than that of MGF ($2108\ m^2\ g^{-1}$). However, the ECSA values of NMGF and MGF are similar, indicating a better hydrophilicity of NMGF. The similar ECSA of NMGF and MGF also demonstrates that, for NMGF and MGF, the surface area exposed to the electrolyte are similar, thus the catalytic activity mainly depends on the quantity of active sites on the surface. Therefore, the ECSA test further confirms that the superior activity of NMGF to MGF is attributed to the N doping, which brings more active sites to NMGF.

The hydrophilicity can also be quantitatively described by the contact angle. Fig. 4d exhibits the contact angle tests of NMGF and MGF samples using deionized water as the wetting liquid. With the introduction of N heteroatoms, the contact angle is greatly decreased from 85.9° to 64.3°, demonstrating a remarkably improved surface wettability and thereby an enhanced electrolyte permeation and affinity. The contact angle of NG shown in Fig. S7 is 58.2°, confirming that the hydrophilic surface is attributed to the N doping. Benefitting from the active centers contributed by interconnected pores and superb hydrophilicity, NMGF affords prominent superiority in terms of enhancing the exposure of active sites.

With abundant effective active centers contributed by heteroatoms and defects, the unique 3D mesoporous framework and hydrophilic surface, as well as the enhanced electron/ion conductivity, NMGF exhibits impressive activity on the bifunctional catalysis of ORR and OER. Such NMGF is also expected to be served as electrocatalyst for other multi-electron redox reactions [48] and conductive hosts for polar intermediate anchoring in a working Li-S batteries [49,50], which is a novel energy material platform to modulate the kinetic of oxidation/reduction and diffusion of intermediates in an electrochemical energy conversion system.

## 4. Conclusions

The NMGF was synthesized through a CVD method on 3D MgO templates. The as-obtained NMGF with interconnected 5–8 nm mesopores have a N and O content of 3.41 and 3.34 at.%, respectively, an electron conductivity of $57.0\ S\ cm^{-1}$, a surface area of $1440\ m^2\ g^{-1}$, and a pore volume of $2.18\ cm^3\ g^{-1}$. Such unique structural features render NMGF as an efficient bifunctional catalyst for ORR and OER. The NMGF catalyst exhibits a low OER-ORR potential gap of 0.95 V, which is much smaller than the routine noble metal catalysts ($IrO_2$, Pt/C), non-doped MGF and GO-derived doped graphene. The NMGF material is promising for practical applications like Zn-air batteries, and it can also be an excellent substrate for the growth of other metal-based materials with further enhanced performance. The structure design strategy of maintaining the conductivity of porous material can be instructive for the future investigation on electrocatalysis and other energy storage systems based on multi electron redox reaction.

## Acknowledgements

This work was supported by the National Key Research and Development Program (Nos. 2016YFA0202500 and 2016YFA0200101) and the Natural Scientific Foundation of China (No. 21422604). The authors thank helpful discussion from Xiang Chen, Bo-Quan Li, Jing-Qi Nie, Chen-Yu Chen, Gui-Li Tian, and Fei Wei.

## Appendix A. Supplementary data

Supplementary data associated with this article can be found, in the online version, at http://dx.doi.org/10.1016/j.cattod.2017.02.012.

## References

[1] L. Wei, D.S. Yu, H.E. Karahan, O. Birer, K. Goh, Y. Yuan, W.C. Jiang, W. Liang, Y. Chen, Catal. Today 249 (2015) 228–235.
[2] Y. Nie, L. Li, Z.D. Wei, Chem. Soc. Rev. 44 (2015) 2168–2201.
[3] J.T. Zhang, H.L. Li, P.Z. Guo, H.Y. Ma, X.S. Zhao, J. Mater. Chem. A 4 (2016) 8497–8511.
[4] C. Tang, H.F. Wang, X.L. Zhu, B.Q. Li, Q. Zhang, Part. Part. Syst. Charact. 33 (2016).
[5] D.W. Wang, D.S. Su, Energy Environ. Sci. 7 (2014) 576–591.
[6] B.-Q. Li, C. Tang, H.-F. Wang, X.-L. Zhu, Q. Zhang, Sci. Adv. 2 (2016) e1600495.
[7] H.B. Yang, J. Miao, S.-F. Hung, J. Chen, H.B. Tao, X. Wang, L. Zhang, R. Chen, J. Gao, H.M. Chen, L. Dai, B. Liu, Sci. Adv. 2 (2016) e1501122.
[8] D.U. Lee, P. Xu, Z.P. Cano, A.G. Kashkooli, M.G. Park, Z. Chen, J. Mater. Chem. A 4 (2016) 7107–7134.
[9] Y.C. Tu, D.H. Deng, X.H. Bao, J. Energy Chem. 25 (2016) 957–966.
[10] S. Chen, J. Duan, Y. Zheng, X. Chen, X.W. Du, M. Jaroniec, S.-Z. Qiao, Energy Storage Mater. 1 (2015) 17–24.
[11] G.L. Tian, Q. Zhang, B.S. Zhang, Y.G. Jin, J.Q. Huang, D.S. Su, F. Wei, Adv. Funct. Mater. 24 (2014) 5956–5961.
[12] G.R. Zhang, M. Munoz, B.J.M. Etzold, Angew. Chem. Int. Ed. 55 (2016) 2257–2261.
[13] U.A. Paulus, T.J. Schmidt, H.A. Gasteiger, R.J. Behm, J. Electroanal. Chem. 495 (2001) 134–145.
[14] T. Reier, M. Oezaslan, P. Strasser, ACS Catal. 2 (2012) 1765–1772.
[15] Y. Lee, J. Suntivich, K.J. May, E.E. Perry, Y. Shao-Horn, J. Phys. Chem. Lett. 3 (2012) 399–404.
[16] L.Z. Yuan, Z. Yan, L.H. Jiang, E.D. Wang, S.L. Wang, G.Q. Sun, J. Energy Chem. 25 (2016) 805–810.
[17] I. Katsounaros, S. Cherevko, A.R. Zeradjanin, K.J.J. Mayrhofer, Angew. Chem. Int. Ed. 53 (2014) 102–121.
[18] Y. Gorlin, T.F. Jaramillo, J. Am. Chem. Soc. 132 (2010) 13612–13614.
[19] K.L. Pickrahn, S.W. Park, Y. Gorlin, H.B.R. Lee, T.F. Jaramillo, S.F. Bent, Adv. Energy Mater. 2 (2012) 1269–1277.
[20] M. Hamdani, R.N. Singh, P. Chartier, Int. J. Electrochem. Sci. 5 (2010) 556–577.
[21] Y. Gorlin, B. Lassalle-Kaiser, J.D. Benck, S. Gul, S.M. Webb, V.K. Yachandra, J. Yano, T.F. Jaramillo, J. Am. Chem. Soc. 135 (2013) 8525–8534.
[22] F.Y. Cheng, J.A. Shen, B. Peng, Y.D. Pan, Z.L. Tao, J. Chen, Nat. Chem. 3 (2011) 79–84.
[23] G.L. Tian, M.Q. Zhao, D.S. Yu, X.Y. Kong, J.Q. Huang, Q. Zhang, F. Wei, Small 10 (2014) 2251–2259.
[24] R.M. Yadav, J.J. Wu, R. Kochandra, L.L. Ma, C.S. Tiwary, L.H. Ge, G.L. Ye, R. Vajtai, J. Lou, P.M. Ajayan, ACS Appl. Mater. Interfaces 7 (2015) 11991–12000.
[25] R. Li, Z.D. Wei, X.L. Gou, ACS Catal. 5 (2015) 4133–4142.
[26] Y. Jia, L. Zhang, A. Du, G. Gao, J. Chen, X. Yan, C.L. Brown, X. Yao, Adv. Mater. 28 (2016) 9532–9538.
[27] C. Tang, H.F. Wang, X. Chen, B.Q. Li, T.Z. Hou, B.S. Zhang, Q. Zhang, M.M. Titirici, F. Wei, Adv. Mater. 28 (2016) 6845–6851.
[28] J.T. Zhang, Z.H. Zhao, Z.H. Xia, L.M. Dai, Nat. Nanotechnol. 10 (2015) 444–452.
[29] Y.F. Jiang, L.J. Yang, T. Sun, J. Zhao, Z.Y. Lyu, O. Zhuo, X.Z. Wang, Q. Wu, J. Ma, Z. Hu, ACS Catal. 5 (2015) 6707–6712.
[30] S. Chen, J.J. Duan, M. Jaroniec, S.Z. Qiao, Adv. Mater. 26 (2014) 2925–2930.
[31] Y.G. Li, W. Zhou, H.L. Wang, L.M. Xie, Y.Y. Liang, F. Wei, J.C. Idrobo, S.J. Pennycook, H.J. Dai, Nat. Nanotechnol. 7 (2012) 394–400.
[32] S.W. Liu, H.M. Zhang, Q. Zhao, X. Zhang, R.R. Liu, X. Ge, G.Z. Wang, H.J. Zhao, W.P. Cai, Carbon 106 (2016) 74–83.
[33] X.Q. Zhang, X.B. Cheng, Q. Zhang, J. Energy Chem. 25 (2016) 967–984.
[34] J. Wang, Z.X. Wu, L.L. Han, Y.Y. Liu, J.P. Guo, H.L.L. Xin, D.L. Wang, Chin. Chem. Lett. 27 (2016) 597–601.
[35] L.P. Wang, W.S. Jia, X.F. Liu, J.Z. Li, M.M. Titirici, J. Energy Chem. 25 (2016) 566–570.
[36] C. Tang, H.S. Wang, H.F. Wang, Q. Zhang, G.L. Tian, J.Q. Nie, F. Wei, Adv. Mater. 27 (2015) 4516–4522.
[37] H.J. Peng, D.W. Wang, J.Q. Huang, X.B. Cheng, Z. Yuan, F. Wei, Q. Zhang, Adv. Sci. 3 (2016) 1500268.
[38] H. Terrones, A.L. Mackay, Carbon 30 (1992) 1251–1260.
[39] Q. Liu, J.T. Jin, J.Y. Zhang, ACS Appl. Mater. Interfaces 5 (2013) 5002–5008.
[40] A. Aijaz, J. Masa, C. Rosler, W. Xia, P. Weide, A.J.R. Botz, R.A. Fischer, W. Schuhmann, M. Muhler, Angew. Chem. Int. Ed. 55 (2016) 4087–4091.
[41] Y. Wang, W. Ding, S.G. Chen, Y. Nie, K. Xiong, Z.D. Wei, Chem. Commun. 50 (2014) 15529–15532.
[42] K. Gong, F. Du, Z. Xia, M. Durstock, L. Dai, Science 323 (2009) 760–764.
[43] C. Tang, Q. Zhang, Adv. Mater. 29 (2017) 1604103.
[44] R.S. Zhong, Y.H. Qin, D.F. Niu, J.W. Tian, X.S. Zhang, X.G. Zhou, S.G. Sun, W.K. Yuan, J. Power Sources 225 (2013) 192–199.
[45] Y. Jiao, Y. Zheng, M. Jaroniec, S.Z. Qiao, J. Am. Chem. Soc. 136 (2014) 4394–4403.

[46] X. Lu, W.-L. Yim, B.H.R. Suryanto, C. Zhao, J. Am. Chem. Soc. 137 (2015) 2901–2907.
[47] L.P. Zhang, Q. Xu, J.B. Niu, Z.H. Xia, Phys. Chem. Chem. Phys. 17 (2015) 16733–16743.
[48] D.S. Su, S. Perathoner, G. Centi, Chem. Rev. 113 (2013) 5782–5816.
[49] J.-Q. Huang, Q. Zhang, F. Wei, Energy Storage Mater. 1 (2015) 127–145.
[50] T.Z. Hou, X. Chen, H.J. Peng, J.Q. Huang, B.Q. Li, Q. Zhang, B. Li, Small 12 (2016) 3283–3291.